Progress In Electromagnetics Research M, Vol. 113, 163–172, 2022

Design and Analysis of a Wireless Power Transmitting System for Capsule Robot Using Two-Dimensional Combined Solenoid Coils

Chen Gao[1], Jinyang Gao[1, 2, *], Changshun Yuan[3], Jinshan Zhou[1], Siyu Tian[1], and Peng Huang[1]

Abstract—Wireless power transmission system (WPTS) based on electromagnetic induction is a promising way to power a gastrointestinal capsule robot (CR) for wireless diagnosis, which typically consists of a one-dimensional (1-D) power transmitting coil (PTC) to excite an alternating magnetic field and a three-dimensional (3-D) power receiving coil (PRC) to induce signal. However, it is difficult to apply a 3-D PRC to practical medical applications since the oversize bodily form of the mounting receiver brings the extra challenge of design for microCR. This paper proposes a novel WPTS with a space-saving architecture by combining a two-dimensional (2-D) PTC outside the human and 1-D PRC onboard the CR, which can permit CR to accomplish the mission of exploring the intestinal space with wireless energy supplying owing to small size related to 1-D PTC. The analytical expressions of the magnetic flux density, magnetic field orientation, and uniform magnetic field excited by the designed PTC are derived. Simulated and experimental outcomes are implemented to achieve the desired magnetic field strength and direction by changing the transmission current of PTC, which verifies the feasibility and effectiveness of developed methods. And the magnetic field uniformity is greater than 44%. It can basically cover the 20 cm × 20 cm area of the human abdomen at all times, which can permit the operational requirements of the CR in the practical case.

1. INTRODUCTION

A capsule robot (CR) is a noninvasive device that can perform gastrointestinal treatment and comprehensive diagnosis by actively moving, which offers remarkable advantages over traditional endoscopes, such as less trauma, straightforward operation, and no pain for the patient [1–4]. Energy supply is a severe bottleneck restricting the CR development in the realistic scenario [5]. The unexpected friction caused by the power cable will weaken the CR movement performance while the risk of intestinal hurt and infection will inevitably increase. The energy provided by the onboard battery is insufficient to power the CR for the long-period mission since the powering capacity is directly related to its volume [6]. Notably, wireless power transmission (WPT) technology based on electromagnetic induction is considered the most promising solution to the energy supply problem of CR, on account of small size, long-term supply, and low risk [7, 8].

The wireless power transmission technology system (WPTS) is composed of two components: a power transmitting coil (PTC) to provide an alternating magnetic field around the human body and a power receiving coil (PRC) associated with the CR via an inductive linking of the magnetic field. Obviously, the CR needs to reduce the received power fluctuation during the movement in the intestine, thus it requires high uniformity of the magnetic field generated by the WPTS. Recently, a number

---

Received 25 June 2022, Accepted 29 August 2022, Scheduled 20 September 2022

[*] Corresponding author: Jinyang Gao (gjy.1001@163.com).

[1] State Key Laboratory of Dynamic Measurement Technology, North University of China, Taiyuan 030051, China. [2] Shanxi Key Laboratory of Advanced Manufacturing Technology, North University of China, Taiyuan 030051, China. [3] Hangzhou Innovation Institute, Beihang University, Hangzhou 310051, China.

of researches concerning the construction and optimization of WPTS have been reported, aiming to accomplish a steady power supply for the CR by properly building the transmission system [9–16]. A pair of Helmholtz coils is employed to realize a high uniformity of the magnetic field inside PTC [9], and a three-dimensional (3-D) PRC is loaded in CR to obtain the energy. A WPTS consists of a 1-D PTC which excites the magnetic field and a 3-D PRC which is utilized to induct it [10]. Moreover, many methods related to optimizing the structure of 1-D PRC and 3-D PRC have been presented [12–14]. However, the above mentioned literature findings [9–14] are difficult to be directly taken into realistic scenes due to the large size of the 3-D PRC attached to CR. It should be noted that the diameter of the narrowest part is approximately 15 mm in the small intestine for adults; thus, the volume of CR must be strictly regulated so that CR can be well operated in the intestine [15]. Fortunately, by using a 1-D PRC, the size of CR can be significantly reduced, resulting in better space utilization. However, it is worth noting that in order to obtain maximum power from a 1-D PTC, the CR equipped with a 1-D PRC must be aligned with the direction of the magnetic field during operation [16]. However, it is difficult to maintain the uniform direction with the magnetic field for CR during the term of moving because the intestine path existing in the body is tortuous, which leads to the uncoupled state of the entire system, rendering the power of CR receiving less or even no power at all, thus the stability and feasibility of WPTS may be decreased. According to the anatomy of the intestinal, the route of CR movement in the human intestine is roughly modeled as a plane with a pitch angle of 30° or less, meaning that PTC only requires to be designed as a controlled directional magnetic field in the 2-D plane to satisfy the energy requirements of CR [17]. Therefore, it is necessary to develop a WPTS compared with the traditional transmission system of 2-D PTC and 1-D PRC so that it can perform related operations in the complex human intestine, which stimulates us to provide satisfying solutions.

Inspired by the above observations, this paper proposes a novel WPTS consisting of a 2-D PTC and 1-D PRC with a spacing-saving architecture. Based on the WPT and Biot-Savart Law, the PTC is designed by combining a pair of square and circular solenoid coils to accomplish a uniform magnetic field in the abdominal area of a human, which can fulfill the realistic requirement in the medical field. Firstly, the model's magnetic flux density, magnetic field orientation, and high uniformity area are calculated theoretically. Secondly, finite element simulation software is utilized to verify the feasibility of the proposed scheme. Thirdly, the experiment is conducted to find that the presented combination based on 2-D PTC could provide stable power to the CR.

This article is organized as follows. Section 2 explains the working mechanism of the WPTS. Section 3 describes the PTC structure and develops a theoretical calculation model of its magnetic field. Simulation and experiment outcomes are illustrated in Section 4. Concludes are discussed in Section 5.

2. WORKING MECHANISM OF WPTS

The equivalent circuit of the WPTS based on electromagnetic induction is shown in Figure 1, which includes a transmitting circuit and a receiving circuit.

The transmitting circuit is outside the body and consists of three parts: a signal generator, a

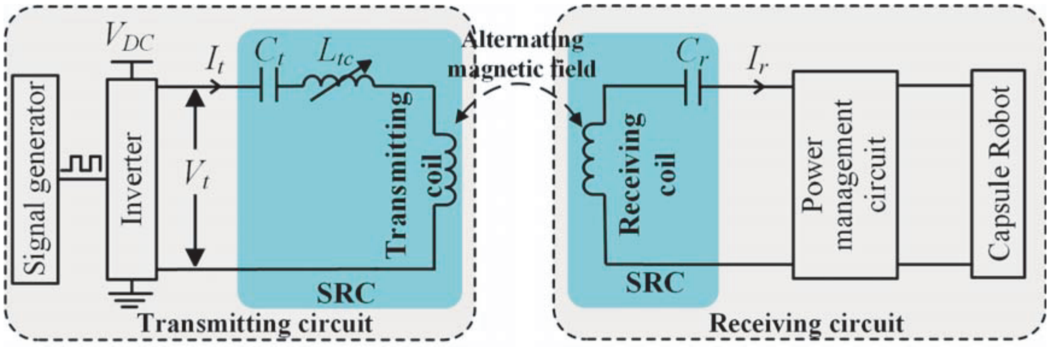

Figure 1. Equivalent circuit of the WPTS.

full-bridge inverter, and a serial resonant circuit (SRC). The signal generator generates a square wave signal, and the full-bridge inverter converts the DC voltage V_{DC} to AC voltage V_t under the control of the square wave signal. The SRC consists of a resonant capacitor C_t, an adjustable inductor L_{tc}, and a pair of PTCs. In this case, C_t and L_{tc} make the PTC resonate at a specific frequency f. When an AC pulse voltage V_t is applied to the SRC, a sinusoidal excitation current I_t is generated in the PTC, which will excite an alternating magnetic field.

The receiving circuit is integrated inside the CR and consists of two parts: an SRC and a power management circuit. The SRC consists of the PRC and a resonant capacitor C_r where the latter makes the PRC resonate at the frequency f. The PRC is in an alternating magnetic field to obtain the induced electric potential [18], applying to the gastrointestinal CR through an energy management circuit.

3. ANALYSIS OF 2-D PTC

3.1. Structure Design of 2-D PTC

Figure 2 illustrates the relative position relation between the human abdominal model and the CR. The 2-D PTC is designed by an outside coil pair A and an inside coil pair B, as shown in Figure 3. Square coils are utilized to facilitate easy installation of the PTC and accommodate the body size on the outside, where the side length of the square coil is $2L_A = 44\,\text{cm}$, and the center distance is $2D_A = 38\,\text{cm}$. The coil pair B is set as a circular coil on the inside to enable a better fit since the abdominal region of the patient is oval. Moreover, to facilitate the implementation, the coil should be as small as possible, so it can be operated flexibly. Thus, the radius $L_B = 20\,\text{cm}$ can accommodate the large majority of adult males for circular coils. Helmholtz-type coils can maximize the uniformity of the magnetic field, i.e., circular coils spaced $2D_B = 20\,\text{cm}$ apart at the center of the magnet. The number of turns of single side coil is $n_A = n_B = 25$ for both coils.

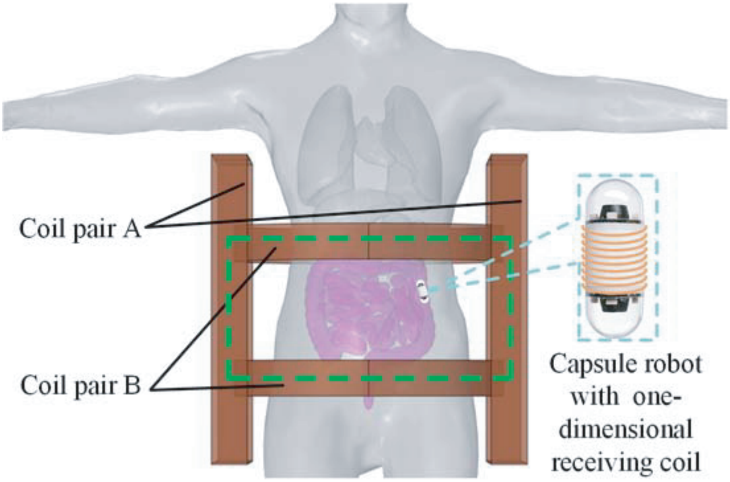

Figure 2. Relative position relation between the human abdominal model and CR.

3.2. Analysis of the Magnetic Flux Density

Figure 3 shows the simplified coil model of the PTC. The vectors $\vec{r}_i$, $\vec{r}_j$, $\vec{r}_p$, and $\vec{r}_q$ are from any point $P\ (x, y, 0)$ in the XOY plane to the current micro-element $I_A dl_i$, $I_A dl_i$, $I_B dl_p$, and $I_B dl_q$; θ_i, θ_j, θ_p, and θ_q are the angles of the current micro-element with the point P. The CR moves in the largest plane roughly parallel to the rectangle (i.e., the $z = 0$ plane), and the magnetic flux density (MFD) in this plane is analyzed. For other planes, the system presents a similar behavior.

Using the Biot-Savart Law, the MFD B_P at the point P is equal to the vector sum of the four coils

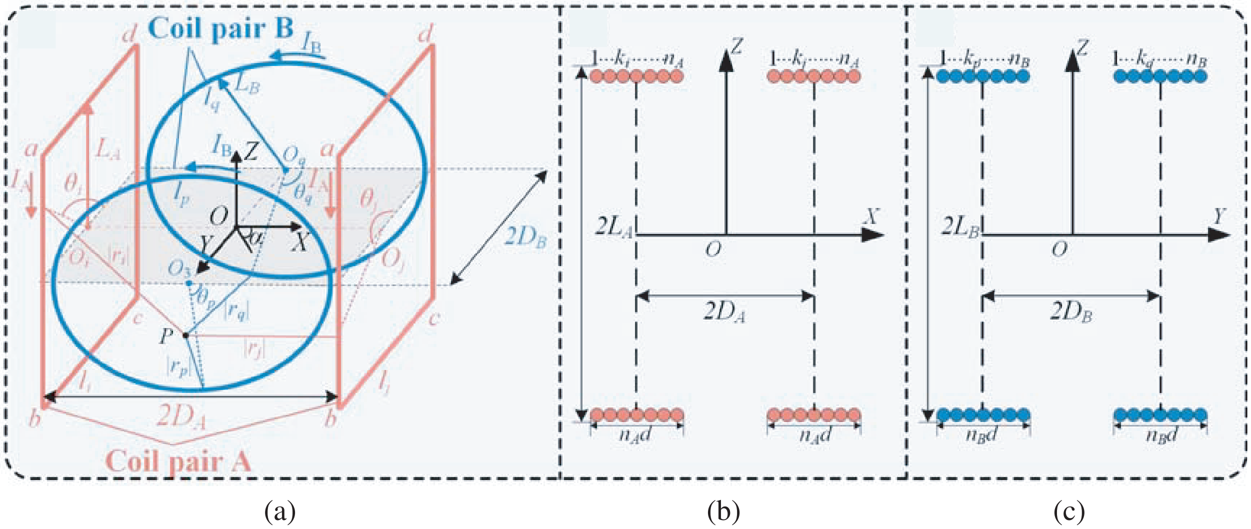

Figure 3. (a) The simplified PTC model, (b) the complete coil model of the square coils, and (c) the complete coil model of the circular coils.

MFD in the XOY plane, where $\mu_0 = 4\pi \times 10^{-7}$ H/m is the vacuum magnetic permeability.

$$\vec{B}_P = \frac{n_A\mu_0}{4\pi}\left(\int_{li}\frac{I_A d\vec{l}_i \times \vec{r}_i}{|r_i|^3} + \int_{lj}\frac{I_A d\vec{l}_j \times \vec{r}_j}{|r_j|^3}\right) + \frac{n_B\mu_0}{4\pi}\left(\int_{lp}\frac{I_B d\vec{l}_p \times \vec{r}_p}{|r_p|^3} + \int_{lq}\frac{I_B d\vec{l}_q \times \vec{r}_q}{|r_q|^3}\right) \tag{1}$$

When coil pair A operates alone, the $\vec{B}_p$ is along the X-axis; when coil pair B is performed alone, the $\vec{B}_p$ is along the Y-axis; when the coil pairs A and B work simultaneously, the direction produced is the vector sum of X and Y directions:

$$\vec{B}_P = \vec{B}_x + \vec{B}_y \tag{2}$$

3.2.1. The MFD of the Coil Part A

As shown in Figures 3(a) and (b), the coil part A is divided into four segments at each turn: ad, dc, cb, and ba. At the i-th turn to the left half of coil part A, the angle between the XOY plane and each section (ad, dc, cb, and ba) is denoted as θ_i, and the coordinates of the infinitesimal current $I_A d\vec{l}_i$ are $((i-\frac{n+1}{2})d - D_A, -L_A, -L_A\tan\theta_i)$, $((i-\frac{n+1}{2})d - D_A, -L_A\cot\theta_i, -L_A)$ and $((i-\frac{n+1}{2})d - D_A, L_A, L_A\tan\theta_i)$; the components of infinitesimal current $I_A d\vec{l}_i$ are $(0, -I_A L_A\csc^2\theta_i d\theta_i, 0)$, $0, 0, -I_A L_A\sec^2\theta_i d\theta_i$, $(0, I_A L_A\csc^2\theta_i d\theta_i, 0)$ and $(0, 0, I_A L_A\sec^2\theta_i d\theta_i)$. The vectors from any point P $(x, y, 0)$ to the infinitesimal current $I_A d\vec{l}_i$ are $\vec{r}_{i\_1}$, $\vec{r}_{i\_2}$, $\vec{r}_{i\_3}$, and $\vec{r}_{i\_4}$, where the coordinates are $((i-\frac{n+1}{2})d - D_A - x, L_A\cot\theta_i - y, L_A)$, $((i-\frac{n+1}{2})d - D_A - x, -L_A - y, -L_A\tan\theta_i)$, $((i-\frac{n+1}{2})d - D_A - x, -L_A\cot\theta_i - y, -L_A)$, and $((i-\frac{n+1}{2})d - D_A - x, L_A - y, L_A\tan\theta_i)$, respectively. Therefore, the MFD at point P in the left half of coil part A can be calculated as follows:

$$B_{x\_i} = \frac{\mu_0 I_A}{4\pi}\sum_{k_i=1}^{n_A}\left(\begin{array}{l} \displaystyle\int_{\pi/4}^{3\pi/4}\frac{-L_A^2\csc^2\theta_i}{|r_{i\_1}|^3}d\theta_i + \int_{3\pi/4}^{5\pi/4}\frac{\left(-L_A y\sec^2\theta_i - L_A^2\sec^2\theta_i\right)}{|r_{i\_2}|^3}d\theta_i \\ \displaystyle + \int_{5\pi/4}^{7\pi/4}\frac{-L_A^2\csc^2\theta_i}{|r_{i\_3}|^3}d\theta_i + \int_{7\pi/4}^{9\pi/4}\frac{\left(L_A y\sec^2\theta_i - L_A^2\sec^2\theta_i\right)}{|r_{i\_4}|^3}d\theta_i \end{array}\right) \tag{3}$$

Consistent with the left half, at the j-th turn to the right half of coil part A, the angle between the XOY plane and each section (ad, dc, cb, and ba) is denoted as θ_j, and the coordinates of the infinitesimal current $I_A d\vec{l}_j$ are $((j-\frac{n+1}{2})d+D_A, L_A\cot\theta_j, L_A)$, $((j-\frac{n+1}{2})d+D_A, -L_A, -L_A\tan\theta_j)$, $((j-\frac{n+1}{2})d+D_A, -L_A\cot\theta_j, -L_A)$ and $((j-\frac{n+1}{2})d+D_A, L_A, L_A\tan\theta_j)$; the three components of infinitesimal current $I_A d\vec{l}_j$ are $(0, -I_A L_A\csc^2\theta_j d\theta_j, 0)$, $(0, 0, -I_A L_A\sec^2\theta_j d\theta_j)$, $(0, I_A L_A\csc^2\theta_j d\theta_j, 0)$ and $(0, 0, I_A L_A\sec^2\theta_j d\theta_j)$. The vectors from any point P $(x, y, 0)$ to the infinitesimal current $I_A d\vec{l}_j$ are $\vec{r}_{j\_1}$, $\vec{r}_{j\_2}$, $\vec{r}_{j\_3}$, and $\vec{r}_{j\_4}$ with the coordinates are $((j-\frac{n+1}{2})d+D_A-x, L_A\cot\theta_j-y, L_A)$, $((j-\frac{n+1}{2})d+D_A-x, -L_A-y, -L_A\tan\theta_j)$, $((j-\frac{n+1}{2})d+D_A-x, -L_A\cot\theta_j-y, -L_A)$, and $((j-\frac{n+1}{2})d+D_A-x, L_A-y, L_A\tan\theta_j)$, respectively. Therefore, the MFD at point P in the right half of coil part A can be calculated as follows:

$$B_{x\_j} = \frac{\mu_0 I_A}{4\pi}\sum_{k_j=1}^{n_A}\left(\begin{array}{l} \displaystyle\int_{\pi/4}^{3\pi/4}\frac{-L_A^2\csc^2\theta_j}{|r_{j\_1}|^3}d\theta_j + \int_{3\pi/4}^{5\pi/4}\frac{\left(-L_A y\sec^2\theta_j - L_A^2\sec^2\theta_j\right)}{|r_{j\_2}|^3}d\theta_j \\ \displaystyle + \int_{5\pi/4}^{7\pi/4}\frac{-L_A^2\csc^2\theta_j}{|r_{j\_3}|^3}d\theta_j + \int_{7\pi/4}^{9\pi/4}\frac{\left(L_A y\sec^2\theta_j - L_A^2\sec^2\theta_j\right)}{|r_{j\_4}|^3}d\theta_j \end{array}\right) \tag{4}$$

In the X-axis, the MFD generated by coil part A at point P can be expressed as:

$$B_x = B_{x\_i} + B_{x\_j} \tag{5}$$

3.2.2. The MFD of the Coil Part B

As shown in Figures 3(a) and 3(c), at the p-th turn to the front half of coil part B, the angle is θ_p, and the coordinates of the infinitesimal current $I_B d\vec{l}_p$ are $(L_B\cos\theta_p, (p-\frac{n+1}{2})d-D_B, L_B\sin\theta_p)$; the components of infinitesimal current $I_B d\vec{l}_p$ are $(-I_B L_B\sin\theta_p d\theta_p, 0, I_B L_B\cos\theta_p d\theta_p)$. The vectors from any point P $(x, y, 0)$ to the infinitesimal current $I_B d\vec{l}_p$ are $\vec{r}_p$, where $\vec{r}_p = (L_B\cos\theta_p - x, (p-\frac{n+1}{2})d + D_B - y, L_B\sin\theta_p)$. Therefore, in the front half of coil part B, the MFD at point P can be calculated as follows:

$$B_{y\_p} = \frac{\mu_0 I_B}{4\pi}\sum_{k_p=1}^{n_B}\int_0^{2\pi}\frac{L_B y\cos\theta_p - L_B^2}{|r_p|^3}d\theta_p \tag{6}$$

Consistent with the front half, at the q-th f turn to the behind halfcoil part B, the angle is θ_q, and the coordinates of the infinitesimal current $I_B d\vec{l}_q$ are $(-I_B L_B\sin\theta_q d\theta_q, 0, I_B L_B\cos\theta_q d\theta_q)$; the components of infinitesimal current $I_B d\vec{l}_q$ are $(-I_B L_B\sin\theta_q d\theta_q, 0, I_B L_B\cos\theta_q d\theta_q)$. The vectors from any point P $(x, y, 0)$ to the infinitesimal current $I_B d\vec{l}_p$ are $\vec{r}_q$, where $\vec{r}_q = (L_B\cos\theta_q - x, (q-\frac{n+1}{2})d - D_B - y, L_B\sin\theta_q)$. Therefore, in the behind half of coil part B, the MFD at point P can be derived as follows:

$$B_{y\_q} = \frac{\mu_0 I_B}{4\pi}\sum_{k_q=1}^{n_B}\int_0^{2\pi}\frac{L_B y\cos\theta_q - L_B^2}{|r_q|^3}d\theta_q \tag{7}$$

On the Y-axis, the MFD excited by coil part B at point P can be expressed as:

$$B_y = B_{y\_p} + B_{y\_q} \tag{8}$$

When the two coils are operated simultaneously, the total MFD is:

$$B_{xy} = \sqrt{B_x^2 + B_y^2} \tag{9}$$

3.3. Analysis of the Magnetic Field Orientation

Magnetic field orientation (MFO) depends on the superimposing direction of the magnetic field generated by coil parts A and B. α denotes the orientation angle between the orientation of the MFO and the X-axis at the moment $t = 0$, which can be deduced as:

$$\alpha = \arctan\frac{B_y}{B_x}(180/\pi)^\circ \tag{10}$$

3.4. Analysis of the Magnetic Field Uniformity

To analyze the homogeneity of the magnetic field, define the magnetic field uniformity as:

$$U_{MFD}(x, y, 0) = \left|1 - \frac{B_P(x, y, 0) - B_{P0}}{B_{P0}}\right| \times 100\% \tag{11}$$

where B_P $(x, y, 0)$ represents the MFD at point P $(x, y, 0)$, and B_{p0} is the MFD at the center point $(0, 0, 0)$. $U \geq 90\%$ is considered a highly uniform magnetic field, and CR can work stably in this region. The proportion η of available area is calculated as:

$$\eta = \frac{S_{available}}{S_{total}} \times 100\% \tag{12}$$

where $S_{available}$ is the largest rectangular region with S_{total} designated by the green dashed line in Figure 2, with the size 40×20 cm.

4. EXPERIMENTS AND RESULTS

4.1. Experimental Setup

To verify the viability of the proposed scheme, the experimental outcomes are delineated in Figure 5. A 2-D transmitting coil type comprising paired circular coils and square coils, whose configuration is shown in Figure 4, is placed at a two-axis rack, which can change the MFD and MFO by turning the current intensity. The Litz wire used for winding each coil is AWG38 which consists of 180 strands. Two driving boxes supply drive current to the coils parts A and B, respectively, which are composed of an adjustable inductance, two switching power supplies (SPS), a signal generator, a power inverter, a resonant capacitor, an ammeter, and a voltmeter.

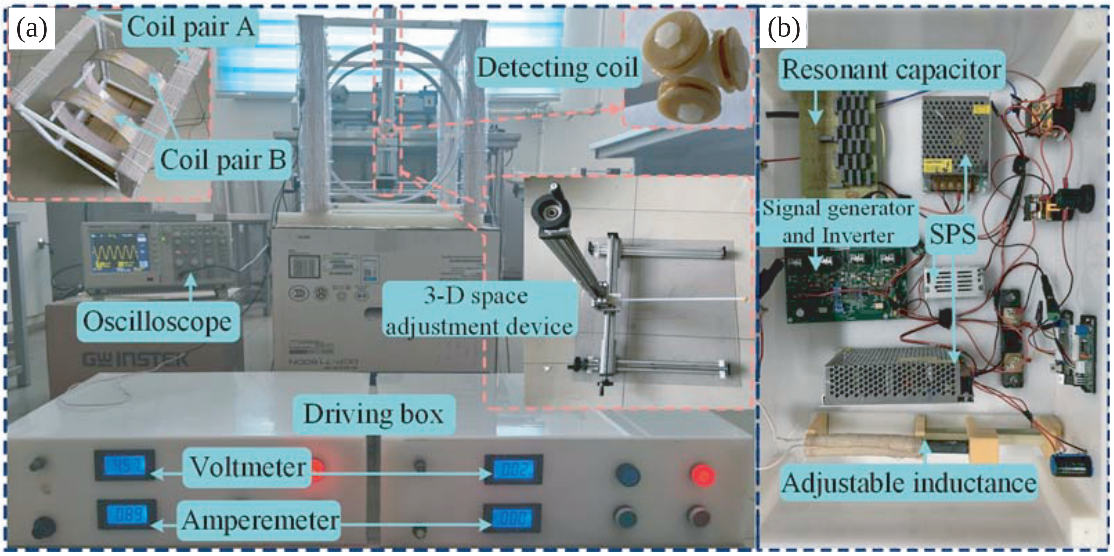

Figure 4. (a) Experimental setup and (b) inside of the drive box.

In the XOY plane, the detection coil can detect the MFD at any position using a 3-D adjustment device. The detecting coil has a diameter of 14 mm and a turn count of 48, which can measure the induced electromotive force in the XOY plane by adjusting the position of the detection coil. Therefore, MDF at point P can be calculated by reading the induction potential of the detecting coil at the oscilloscope by Eq. (13).

$$\varepsilon(x, y, 0) = n\omega S\,|B(x, y, 0)| \tag{13}$$

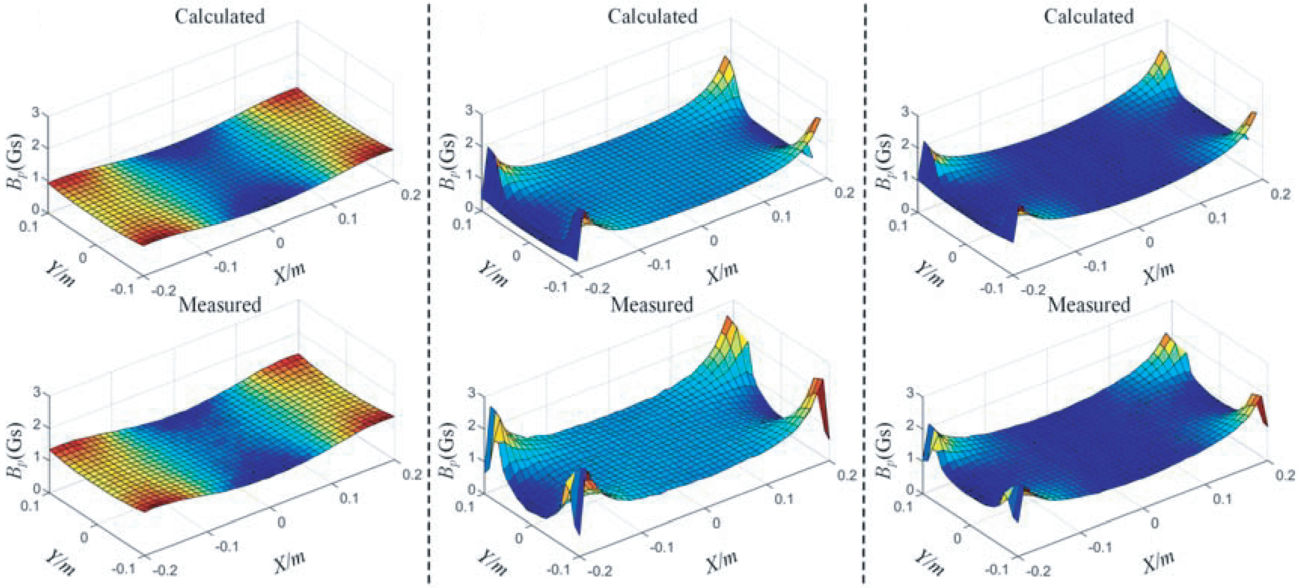

(a) (b) (c)

Figure 5. Calculated and measured values of MFD, (a) $I_A = 1.61\,\text{A}$, $I_B = 0\,\text{A}$, (b) $I_A = 0\,\text{A}$, $I_B = 0.89\,\text{A}$ and (c) $I_A = 1.14\,\text{A}$, $I_B = 0.63\,\text{A}$.

In this equation $\varepsilon\ (x, y, 0)$ is the induced electromotive force of the test coil at point $P\ (x, y, 0)$; $|B(x, y, 0)|$ is the MFD of the detecting coil at point $P\ (x, y, 0)$; n is the number of turns of the detecting coil; the area of the PRC is S; $\omega(= 2\pi f t)$ is the angular frequency of the alternating magnetic field. In order to improve power transmission efficiency, the transmission frequency of this PTC f has been selected as 218 kHz [19].

Table 1 presents the electrical parameters of the two coils as measured by the LCR (IM3536) instrument.

Table 1. The electrical parameters of coil parts A and B.

The electrical parameters	Coil part A	Coil part B
Quality factor Q	740	643
ESR R_s (Ω)	2.63	2.02
Inductance L_s (mH)	1.295	0.961

4.2. Results and Discussion

The experiment outcomes are obtained by utilizing the experimental setup shown in Figure 4, validating the computational model of MFD, MFO, and the uniformity of the magnetic field. Divide S_{total} into 800 regions, with each area being 1 cm^2, and the induced electromotive force can be measured by the detecting coil in each region. The desired MFD of the center point $O\ (0, 0, 0)$ is set as 1 Gs. According to Eq. (9) and Eq. (10), when magnetic field orientation is defined as $a = 0°$, one can calculate that interrelated currents are $I_A = 1.61\,\text{A}$, $I_B = 0\,\text{A}$; when $a = 90°$, $I_A = 0\,\text{A}$, $I_B = 0.89\,\text{A}$; when $a = 45°$, $I_A = 1.14\,\text{A}$ and $I_B = 0.63\,\text{A}$. By varying the values of I_A and I_B, the magnetic fields can be obtained in different directions, so the CR can obtain maximum energy at any angle as it works.

4.2.1. The Results of the MFD

In this case, MATLAB 2020a is used to calculate Eq. (3) to Eq. (9) to obtain the distribution of MFD. Figure 5 depicts the comparative profiles of calculated and measured results in terms of simulations and experiments, which shows that the measured values of MFD can reasonably approximate the theoretical values. Therefore, the validity of the proposed 2-D PTC is proved.

4.2.2. The Results of the MFO

Table 2. Calculated and measured values of MFD, MFO.

Center	$I_A = 1.61\,\text{A}$, $I_B = 0\,\text{A}$		$I_A = 0\,\text{A}$, $I_B = 0.89\,\text{A}$		$I_A = 1.14\,\text{A}$, $I_B = 0.63\,\text{A}$	
	Calculated	Measured	Calculated	Measured	Calculated	Measured
MFD	1 Gs	1.021 Gs	1 Gs	0.992 Gs	1 Gs	0.995 Gs
MFO	0°	0.15°	90°	89.8°	45°	44.7°

By using the detection coil to measure the MFD, together with Eq. (10), the MFO can be calculated theoretically. The related results of experiments are recorded in Table 2, which imply that the calculated outcomes can be well approached by measured results based on Eq. (9) and Eq. (10). Furthermore, in order to observe the whole distribution of the MFO clearly, with the aid of COMSOL 6.2 software the simulation results of MFO are revealed at $t = 0$ in Figure 6, where the arrows indicate the desired orientation. One can obtain that the MFO remains consistent in a region of $40 \times 20\,\text{cm}$ in the XOY plane at the center of the PTC.

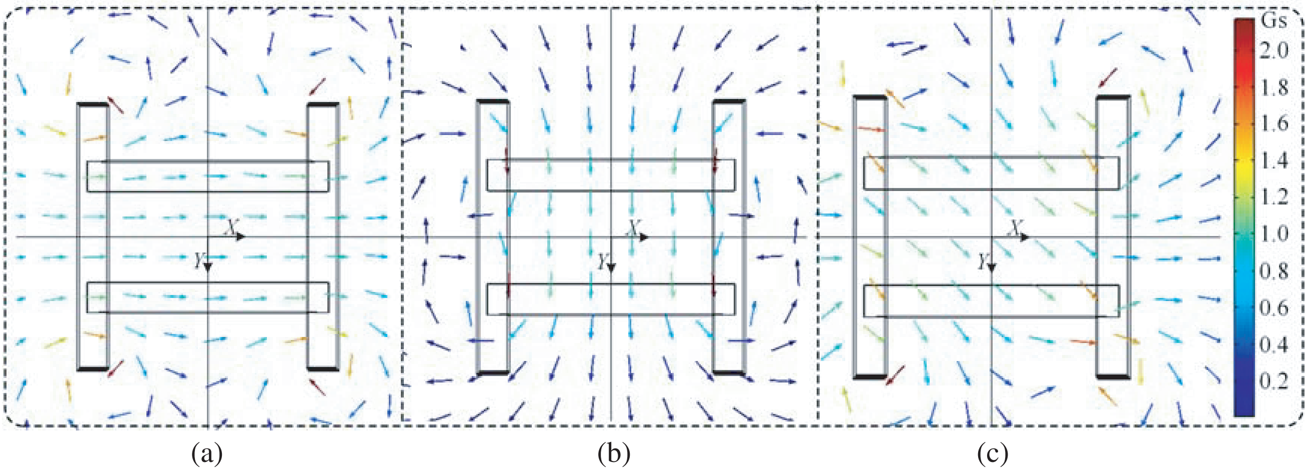

(a) (b) (c)

Figure 6. Simulation results of MFO, (a) $I_A = 1.61\,\text{A}$, $I_B = 0\,\text{A}$, (b) $I_A = 0\,\text{A}$, $I_B = 0.89\,\text{A}$ and (c) $I_A = 1.14\,\text{A}$, $I_B = 0.63\,\text{A}$.

4.2.3. The Results of the Uniformity

In this case, the magnetic field uniformity U_{MFD} is verified by calculation and test. To begin with, define the region $U_{MFD} \geq 90\%$ as red rectangles, as observed in Figure 7. Then, the calculated and measured values of MFD are illustrated in Table 3. It shows that the available area η of red rectangles is always greater than 44%. Thus it can be inferred that uniformity can be well implemented under the scheme of the proposed 2-D PTC in both calculation and test.

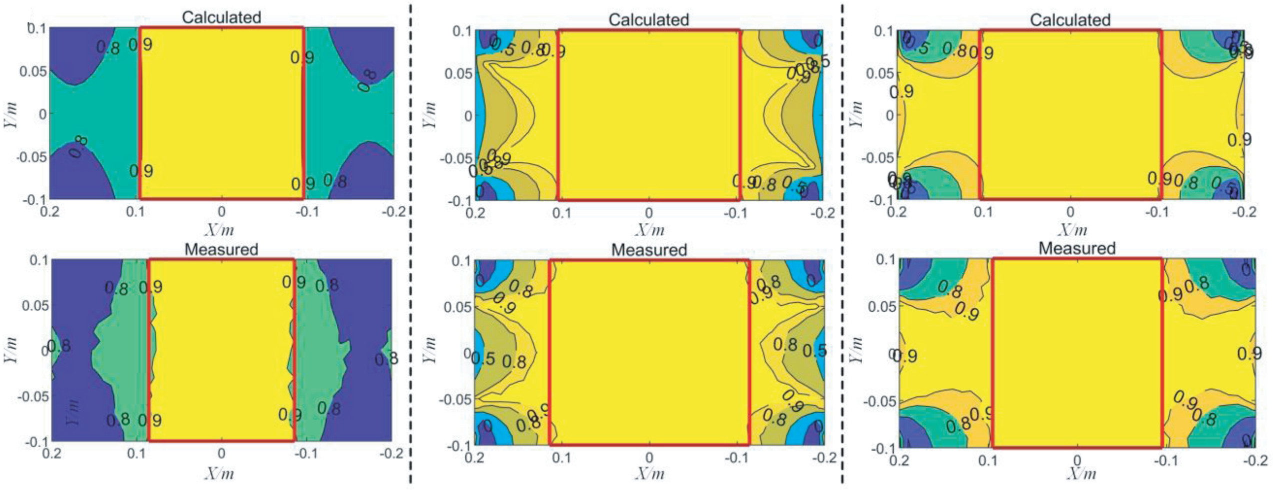

(a) (b) (c)

Figure 7. The U_{MFD} of MFD, (a) $I_A = 1.61$ A, $I_B = 0$ A, (b) $I_A = 0$ A, $I_B = 0.89$ A and (c) $I_A = 1.14$ A, $I_B = 0.63$ A.

Table 3. Calculated and measured values of η.

η	$I_A = 1.61$ A, $I_B = 0$ A		$I_A = 0$ A, $I_B = 0.89$ A		$I_A = 1.14$ A, $I_B = 0.63$ A	
	Calculated	Measured	Calculated	Measured	Calculated	Measured
	46.62%	44%	52.38%	56%	52.38%	49%

5. CONCLUSION

This paper presents a novel wireless power transmitting system with a space-saving architecture by composing 2-D PTC and 1-D PRC for the CR. Based on the Biot-Savart law and WPTS theory, the calculation model of MFD and MFO of the 2-D PTC is established. which can accomplish the appointed orientation and density of the magnetic field with high uniformity and provide the sufficient power to supply the CR. Due to the use of 2-D PTC as opposed to 1-D PTC, the CR onboard 1-D PRC can be designed small so that it will better fit the narrow intestinal tract of patients while decreasing the risk of injury. Simulated and experimental results demonstrate that the desired strength and direction of the magnetic field can be realized well by influencing the transmission current of PTC. And the available uniform magnetic field area supplied to the CR by the PTC is greater than 44%, which can basically cover the area of the human colon region. Thus, the proposed WPTS based on 2-D PTC can provide stable energy supply for gastrointestinal CR, which can meet the operational requirements of power supply for the CR in the practical situation.

ACKNOWLEDGMENT

This work was supported by the National Natural Science Foundation of China (Grant No. 61803347), and supported by the Opening Project of Shanxi Key Laboratory of Advanced Manufacturing Technology (Grant No. XJZZ202101), and supported by the Key Research and Development Plan of Shanxi Province (Grant No. 201903D321164) and supported by the Shanxi Province Science Foundation for Youths (Grant No. 201801D221201) and supported by Scientific and Technological Innovation Programs of Higher Education Institutions in Shanxi (Grant No. 2019L0512), and supported by the Youth Academic Leader Support Project of North University (Grant No. QX201808).

REFERENCES

1. Mapara, S. S. and V. B. Patravale, "Medical capsule robots: A renaissance for diagnostics, drug delivery and surgical treatment," *J. Control Release*, Vol. 261, 337–351, Sep. 2017.
2. Woods, S. P. and T. G. Constandinou, "Wireless capsule endoscope for targeted drug delivery: Mechanics and design considerations," *IEEE Trans. Biomed. Eng.*, Vol. 60, No. 4, 945–953, Apr. 2013.
3. Guo, S., Q. Yang, L. Bai, and Y. Zhao, "Development of multiple capsule robots in pipe," *Micromachines*, Vol. 9, No. 6, 259, May 2018.
4. Jia, Z., G. Yan, H. Liu, Z. Wang, P. Jiang, and Y. Shi, "The optimization of wireless power transmission: Design and realization," *Int. J. Med. Robot*, Vol. 8, No. 3, 337–347, Sep. 2012.
5. Basar, M. R., M. Y. Ahmad, J. Cho, and F. Ibrahim, "Stable and high-efficiency wireless power transfer system for robotic capsule using a modified helmholtz coil," *IEEE Transactions on Industrial Electronics*, Vol. 64, No. 2, 1113–1122, Sep. 2016.
6. Ciuti, G., A. Menciassi, and P. Dario, "Capsule endoscopy: From current achievements to open challenges," *IEEE Reviews in Biomedical Engineering*, Vol. 4, 59–72, 2011.
7. Jia, Z., G. Yan, P. P. Jiang, Z. Wang, and H. Liu, "Efficiency optimization of wireless power transmission systems for active capsule endoscopes," *Physiol. Meas.*, Vol. 32, No. 10, 1561–1573, Oct. 2011.
8. Basar, M. R., M. Y. Ahmad, J. Cho, and F. Ibrahim, "Application of wireless power transmission systems in wireless capsule endoscopy: An overview," *Sensors*, Vol. 14, No. 6, Art. No. 6, Jun. 2014.
9. Basar, Md. R., M. Y. Ahmad, J. Cho, and F. Ibrahim, "An improved wearable resonant wireless power transfer system for biomedical capsule endoscope," *IEEE Transactions on Industrial Electronics*, Vol. 65, No. 10, 7772–7781, 2018.
10. Baser, M. R., M. Y. Ahmad, J. Cho, and F. Ibrahim, "An improved resonant wireless power transfer system with optimum coil configuration for capsule endoscopy," *Sensors and Actuators A: Physical*, Vol. 249, 207–216, 2016.
11. Gao, J., G. Yan, Y. Shi, H. Cao, K. Huang, H. Gao, and J. Liu, "Analysis of connection way of a three-dimensional receiving coil onboard a capsule robot for wireless power transmission," *Progress In Electromagnetics Research M*, Vol. 78, 39–48, 2019.
12. Ke, Q., W. Luo, G. Yan, and K. Yang, "Analytical model and optimized design of power transmitting coil for inductively coupled endoscope robot," *IEEE Transactions on Biomedical Engineering*, Vol. 63, No. 4, 694–706, Apr. 2016.
13. Carta, R., J. Thoné, and R. Puers, "A wireless power supply system for robotic capsular endoscopes," *Sensors and Actuators A: Physical*, Vol. 162, 177–183, Aug. 2010.
14. Zhang, Z., C. Yuan, J. Gao, C. Gao, and and J. Zhou, "Comparison of the uniformity and efficiency of the square and circular helmholtz coils for wireless power transmission system," *Progress In Electromagnetics Research Letters*, Vol. 97, 131–139, 2021.
15. Helander, H. F. and L. Fändriks, "Surface area of the digestive tract — Revisited," *Scand. J. Gastroenterol.*, Vol. 49, No. 6, 681–689, Jun. 2014.
16. Kopparthi, S. and P. Ajmera, "Power delivery for remotely located microsystems," 31–39, May 2004.
17. Monson, J. R. T., et al., "Practice parameters for the management of rectal cancer (revised)," *Dis. Colon. Rectum*, Vol. 56, No. 5, 535–550, May 2013.
18. Lenaerts, B. and R. Puers, "Inductive powering of a freely moving system," *Sensors and Actuators A: Physical*, Vol. 123–124, 522–530, Sep. 2005.
19. Gao, J., G. Yan, Z. Wang, P. Jiang, and D. Liu, "A capsule robot powered by wireless power transmission: Design of its receiving coil," *Sensors and Actuators A: Physical*, Vol. 234, 133–142, Oct. 2015.